Exchange Pathways in Tris-μ-thiolato-Bridged $[Cr_2L_3](ClO_4)_2Cl{\cdot}H_2O{\cdot}MeOH$ (L = 2,6-Bis(aminomethyl)-4-*tert*-butyl-thiophenolate)

Ralph Schenker,[†] Høgni Weihe,[‡] Hans U. Güdel,*[,†] and Berthold Kersting[§]

Departement für Chemie und Biochemie, Universität Bern, Freiestrasse 3, CH-3000 Bern 9, Switzerland, H. C. Ørsted Institutet, Københavns Universitet, Universitetsparken 5, DK-2100 København Ø, Denmark, and Institut für Anorganische und Analytische Chemie, Universität Freiburg, Albertstrasse 21, D-79104 Freiburg, Germany

Received November 30, 2000

From polarized optical absorption and emission spectra of the tris-μ-thiolato bridged $[Cr_2L_3](ClO_4)_2Cl{\cdot}H_2O{\cdot}$MeOH (L = 2,6-bis(aminomethyl)-4-*tert*-butyl-thiophenolate) **1** in the visible and near UV, the exchange splittings of the $^4A_2$ ground and the ^2E and $^2T_1$ excited states are determined. In view of the large Cr−Cr distance of 3.01 Å, the antiferromagnetic ground state splitting with $J = 78$ cm^{-1} ($H = J(\mathbf{S}_A{\cdot}\mathbf{S}_B)$) is large compared to other triply bridged Cr^{3+} dimers. This can be rationalized using a model based on a valence bond approach, in which the exchange splittings are derived from configuration interactions between the ground electron configuration and ligand-to-metal (LMCT) as well as metal-to-metal (MMCT) charge-transfer configurations. It allows us to distinguish the interactions via ligand orbitals from the direct interactions between the metal-centered orbitals. We compare our results with those obtained for the tri-μ-hydroxo-bridged $[Cr_2(OH)_3(tmtame)_2](NO_3)_3$ (tmtame = *N*,*N*′,*N*″-trimethyl-1,1,1-tris(aminomethyl)ethane) **2**. In the latter the interactions via the ligands are negligible, whereas they play an important role in **1**, due to the softness of the sulfur ligand atoms.

1. Introduction

A wide range of compounds containing exchange-coupled Cr^{3+} dimers have been investigated within the past decades,[1] among which triply bridged dimers built of two face-sharing octahedra have attracted special interest due to their high trigonal symmetry. A number of tri-μ-hydroxo-bridged[2−6] as well as fluoro-,[7] chloro-,[8−10] and bromo-bridged[11−13] Cr^{3+} dimers have been reported in the literature. The halo-bridged ones belong to the well-known family of $A_3Cr_2X_9$ (A = Cs^+, Rb^+, K^+, Et_4N^+) compounds. Exchange splittings in the ground state have been derived both from the temperature dependence of magnetic susceptibility and from high-resolution optical spectroscopy at cryogenic temperatures. The exchange interactions between the ions A and B in the ground state of a Cr^{3+} dimer are usually described by the Heisenberg Hamiltonian

$$H = J(\mathbf{S}_A{\cdot}\mathbf{S}_B) \tag{1}$$

where a positive value for the ground state exchange parameter *J* corresponds to an antiferromagnetic splitting. This gives rise to the well-known Landé splitting pattern. For triply bridged Cr^{3+} dimers it has been empirically found that *J* is exponentially dependent on the Cr−Cr distance *R*:[14,15]

$$J = \alpha{\cdot}e^{-\beta R} \tag{2}$$

This is shown in Figure 1, where the solid line corresponds to a least-squares fit to a number of experimental observations J_{exp}[2−8,13] using eq 2, obtaining the phenomenological parameters $\alpha = 1.76 \times 10^{17}$ cm^{-1}, $\beta = 13.14$ Å^{-1}. Equation 2 is based on the assumption that *J* only depends on the Cr−Cr distance *R*, which is a purely geometrical parameter. Contributions to *J* via exchange pathways explicitly involving the bridging ligands are neglected, and the chemical nature of the ligand atoms is thus not considered. Since the ground state of Cr^{3+} is orbitally nondegenerate, the contributions of the different possible exchange pathways to the *J* parameter cannot be obtained from an analysis of the ground state properties only. Hence, optical spectroscopy is the appropriate technique to determine exchange splittings not only within the ground state but also within ligand-field and ligand-to-metal charge-transfer (LMCT) excited states. Furthermore, a model is required which explicitly takes the exchange interactions via the ligands into account.

We measured optical absorption and emission spectra of the tris-μ-thiolato-bridged $[Cr_2L_3](ClO_4)_2Cl{\cdot}H_2O{\cdot}$MeOH (L = 2,6-bis(aminomethyl)-4-*tert*-butyl-thiophenolate) **1** (see Scheme 1) in the visible and near-UV spectral regions. Polarized crystal

* Author for correspondence. E-mail: hans-ulrich.guedel@iac.unibe.ch. Fax: +41 31 631 43 99.
[†] Universität Bern.
[‡] Københavns Universitet.
[§] Universität Freiburg.

(1) McCarthy, P. J.; Güdel, H. U. *Coord. Chem. Rev.* **1988**, *88*, 69.
(2) Riesen, H.; Güdel, H. U. *Mol. Phys.* **1987**, *60*, 1221.
(3) Riesen, H.; Reber, C.; Güdel, H. U.; Wieghardt, K. *Inorg. Chem.* **1987**, *26*, 2747.
(4) Schenker, R.; Weihe, H.; Güdel, H. U. *Inorg. Chem.* **1999**, *38*, 5593.
(5) Glerup, J.; Larsen, S.; Weihe, H. *Acta Chem. Scand.* **1993**, *47*, 1154.
(6) Andersen, P.; Døssing, A.; Larsen, S.; Pedersen, E. *Acta. Chem. Scand.* **1987**, *A41*, 381.
(7) Schenker, R.; Heer, S.; Güdel, H. U.; Weihe, H. *Inorg. Chem.* **2001**, *40*, 1482.
(8) Briat, B.; Russel, M. F.; Rivoal, J. C.; Chapelle, J. P.; Kahn, O. *Mol. Phys.* **1977**, *34*, 1357.
(9) Johnstone, I. W.; Maxwell, K. J.; Stevens, K. W. H. *J. Phys. C: Solid State Phys.* **1981**, *14*, 1297.
(10) Dean, N. J.; Maxwell, K. J. *Mol. Phys.* **1982**, *47*, 551.
(11) Ferrigato, A.; Maxwell, K. J. *J. Phys. Chem. Solids* **1990**, *51*, 157.
(12) Dean, N. J.; Maxwell, K. J.; Stevens, K. W. H.; Turner, R. J. *J. Phys. C: Solid State Phys.* **1985**, *18*, 4505.
(13) Dubicki, L.; Ferguson, J.; Harrowfield, B. *Mol. Phys.* **1977**, *34*, 1545.
(14) Grey, I. E.; Smith, P. W. *Aust. J. Chem.* **1971**, *24*, 73.
(15) Niemann, A.; Bossek, U.; Wieghardt, K.; Butzlaff, C.; Trautwein, A. X.; Nuber, B. *Angew. Chem., Int. Ed. Engl.* **1992**, *31*, 311.

10.1021/ic001350p CCC: $20.00
Published on Web 05/17/2001

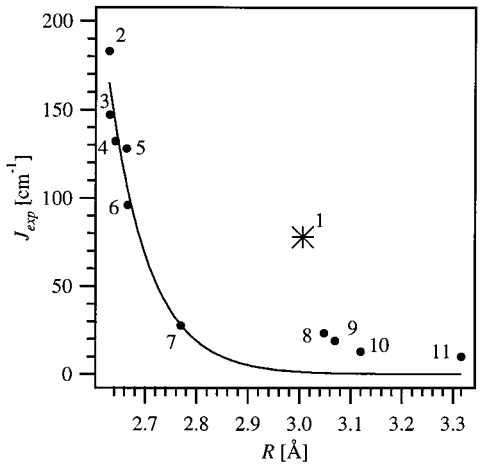

Figure 1. Dependence of the experimental ground state exchange parameter J_{exp} (in cm^{-1}) upon the Cr−Cr distance R (in Å) in tri-μ-bridged Cr^{3+} dimers. The numbered points represent experimental values from the literature. The solid line is a least-squares fit of eq 2 to these data. The asterisk shows the position for the title complex $[Cr_2L_3](ClO_4)_2Cl\cdot H_2O\cdot MeOH$ (**1**). The numbers indicate the following compounds: **2**, $[Cr_2(OH)_3(tmtame)_2](NO_3)_3$, ref 4; **3**, $[Cr_2(OH)_3(tmtame)_2]Cl_3\cdot 4H_2O$, ref 5; **4**, $[Cr_2(OH)_3(NH_3)_6](ClO_4)_{3-x}I_x$, ref 6; **5**, $[Cr_2(OH)_3(tmtacn)_2](ClO_4)_3$, ref 2; **6**, $[Cr_2(OH)_3(tacd)_2]Br_3\cdot 2H_2O$, ref 3; **7**, $(Et_4N)_3Cr_2F_9$, ref 7; **8**, $K_3Cr_2Cl_9$, ref 14; **9**, $Rb_3Cr_2Cl_9$, ref 12; **10**, $Cs_3Cr_2Cl_9$, refs 8 and 9; **11**, $Cs_3Cr_2Br_9$, ref 13.

Scheme 1

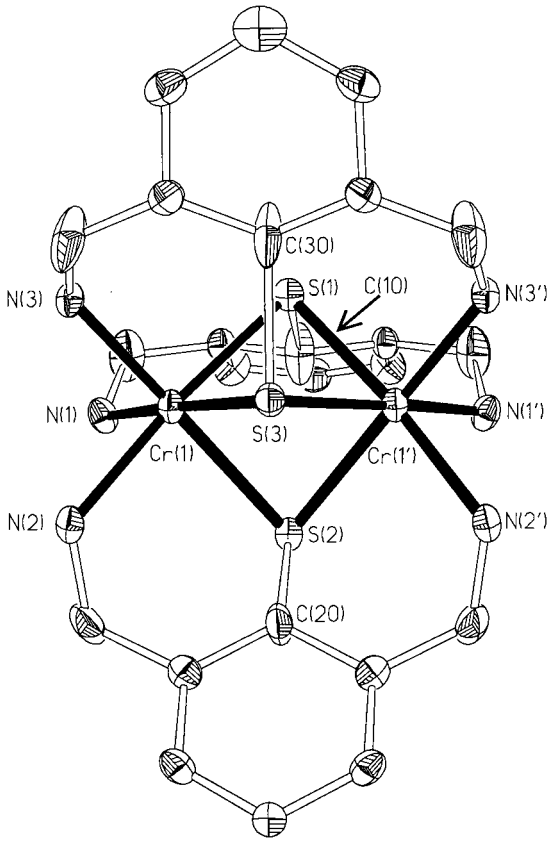

spectra were measured in the region of the $^4A_2 \rightarrow {}^2E$, $^2T_1$ transitions within the t_2 orbitals (O notation). In a dimer these transitions are called single excitations, since formally only one of the two metal centers is excited. The spectra are similar to those of $[Cr_2(OH)_3(tmtame)_2](NO_3)_3$ (tmtame = *N*,*N*′,*N*″-trimethyl-1,1,1-tris(aminomethyl)ethane) **2** reported in ref 4, which allows us to analyze the observed exchange splittings of the ground and singly excited states in comparison. With a ground state exchange parameter $J_{exp} = 78$ cm^{-1} and $R = 3.01$ Å, **1** falls outside the correlation defined by eq 2, which was found for tri-μ-hydroxo- and halo-bridged dimers. This is seen in Figure 1, where the position of **1** is marked with an asterisk. We applied the VBCI model[16] adapted recently for tri-μ-hydroxo-bridged Cr^{3+} dimers[4] to **1**. This model considers LMCT electron configurations explicitly and thus allows us clearly to distinguish the contributions of the different exchange pathways. A comparison of the results for **1** with those reported recently for **2** allows us to investigate the role of the bridging ligands when going from hydroxide to thiolate ligands.

Table 1. Selected Interatomic Distances (in Å) and Angles (deg) for the $[Cr_2L_3]^{3+}$ Cation in **1** Taken from Ref 17[a]

Cr(1)···Cr(1′)	3.009	Cr(1)−Cr(1′)-S(1)	50.5
Cr(1)−S(1)	2.367	Cr(1)−Cr(1′)−S(2)	52.0
Cr(1)−S(2)	2.446	Cr(1)−Cr(1′)−S(3)	50.8
Cr(1)−S(3)	2.382	Cr(1)−Cr(1′)−S(1)−C(10)	112.6
Cr(1)−S(1)−Cr(1′)	78.9	Cr(1)−Cr(1′)−S(2)−C(20)	106.2
Cr(1)−S(2)−Cr(1′)	75.9	Cr(1)−Cr(1′)−S(3)−C(30)	111.7
Cr(1)−S(3)−Cr(1′)	78.3		

[a] The labeling of the atoms refers to Scheme 1. The dihedral angle is defined as the angle between the CrSCr plane and the plane through the adjacent phenyl ring, see Scheme 1.

2. Experimental Section

The title compound $[Cr_2L_3](ClO_4)_2Cl\cdot H_2O\cdot MeOH$ **1** was synthesized as described in ref 17. Deep red single crystals up to 5 mm in length were grown by recrystallization from methanolic solution. They lose solvent upon drying in air. Compound **1** crystallizes in the orthorhombic space group *Cmcm*. The dimeric complex is shown in Scheme 1, where the *tert*-butyl groups and the hydrogen atoms are omitted for clarity. The relevant interatomic distances and angles taken from ref 17 are listed in Table 1. The molecular symmetry is C_s, the mirror plane being the plane defined by the three sulfur atoms. However, for the central core the deviation from D_{3h} symmetry is small. The pseudo-trigonal axis lies parallel to the crystallographic *a* axis, with a Cr−Cr distance of 3.01 Å.

Polarized crystal absorption spectra were measured in the spectral range 770−580 nm in both $E \| a$ and $E \perp a$ polarization, i.e. with the electric vector of the light parallel and perpendicular to the Cr−Cr axis, respectively. For measurements below 580 nm the optical density was too high for crystal measurements, and the compound was dissolved in a 95/5% (v/v) glycerol/water solution, which forms a transparent glass upon cooling. Absorption spectra in the visible and UV were recorded on a double-beam spectrometer, Cary 5e (Varian). Variable sample temperatures between 10 and 150 K were achieved using a closed-cycle helium refrigerator (Air Products). Luminescence of a single crystal was dispersed by a 0.85 m double monochromator (Spex 1402) and detected by a cooled PM tube (RCA 31034) in conjunction with a photon-counting system (SR 400). An Ar^+ laser (Ion Laser Technology 5450A) was used for unselective excitation at 514.5 nm. Selective excitation between 770 and 715 nm was achieved with an Ar^+ laser (Spectra Physics 2060-10 SA) pumped Ti:sapphire laser (Spectra Physics 3900 S). The wavelength was controlled using an inchworm-driven (Burleigh PZ 501) birefringent filter. The spectra were corrected for the sensitivity of the detection system. They are displayed as photon counts versus energy. The sample was cooled to 20 K using a cold helium-gas flow technique.

3. Results

Overview absorption spectra in the visible and near-UV spectral regions of **1** dissolved in a glycerol glass between 20

(16) Tuczek, F. In *Spectroscopic Methods in Bioinorganic Chemistry*; Solomon, E. I., Hodgson, K. E., Eds.; American Chemical Society: Washington, DC, 1998; Chapter 5.
(17) Siedle, G. Diploma Thesis, Universität Freiburg i. Br., Germany, 2000.

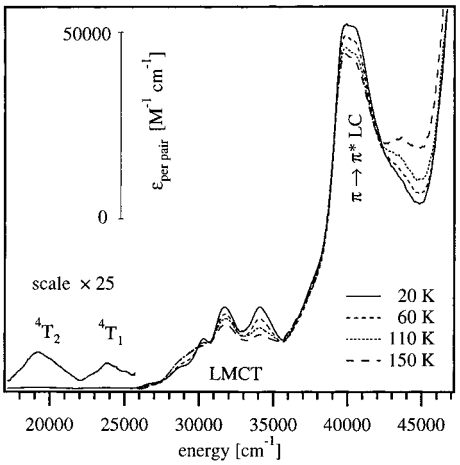

Figure 2. Survey absorption spectra of $[Cr_2L_3](ClO_4)_2Cl\cdot H_2O\cdot MeOH$ dissolved in a glycerol glass in the visible and UV regions at various temperatures between 20 and 150 K as indicated. The ligand-field (note the different scale), LMCT, and ligand-centered (LC) absorptions are labeled.

and 150 K are shown in Figure 2. At 20 K the spectrum is dominated by a very intense broad band centered at 40000 cm^{-1}. Four nicely resolved cold bands are observed between 28000 and 35000 cm^{-1}, which are about an order of magnitude less intense. At higher temperatures, additional hot bands arise at 29000 and 43000 cm^{-1}. Two weak bands are observed at 19000 and 23800 cm^{-1}, which are assigned to the $^4A_2 \rightarrow {}^4T_2$ and $^4A_2 \rightarrow {}^4T_1$ (*O* notation) ligand-field transitions, respectively.

Figure 3 shows single-crystal absorption spectra in $E\perp a$ (top graph) and $E\|a$ (bottom graph) polarizations of $[Cr_2L_3](ClO_4)_2Cl\cdot H_2O\cdot MeOH$ between 12800 and 16500 cm^{-1} at four different temperatures as indicated. The bands arise from $^4A_2 \rightarrow {}^2E$, $^2T_1$ transitions, and their intensities are strongly temperature dependent. Three different temperature dependences are recognized, corresponding to the Boltzmann population of the three lowest ground state dimer levels, which are denoted with their spin quantum numbers *S* in Figure 3. The temperature dependence of the intense hot bands in $E\|a$ polarization is shown in the inset. The hot bands are strongly, but not completely, polarized. In $E\perp a$ polarization the intensity is mainly located between 13000 and 14600 cm^{-1}, in $E\|a$ between 14600 and 15600 cm^{-1}. Energies and predominant polarizations of the observed transitions are listed in Table 2.

Figure 4a shows a comparison of luminescence and luminescence excitation spectra at 20 K as well as the 10 K absorption spectrum in $E\perp a$ polarization. The broad luminescence spectrum on the left (solid line) is obtained upon unselective excitation at 19436 cm^{-1} into the $^4T_2$ absorption band, see Figure 2. Excitation at 13495 cm^{-1}, i.e., below the lowest-energy absorption band, gives rise to the luminescence spectrum shown as a dotted line. Except for the first band at 13320 cm^{-1}, the two spectra are identical, indicating that only the peak at 13320 cm^{-1} is intrinsic, whereas the bulk of the luminescence intensity at lower energy is due to some trap emission. In pure systems excitation energy transfer is very efficient, and small impurities within the ppm range can easily dominate a luminescence spectrum. Further support for this interpretation comes from a comparison of the excitation spectra shown on the right of Figure 4a: detecting the luminescence at 13320 cm^{-1}, the excitation spectrum (solid line) is essentially identical to the 10 K absorption spectrum (thick solid line), whereas detecting the luminescence further in the broad band at 13160 cm^{-1} results in an excitation spectrum (dotted line)

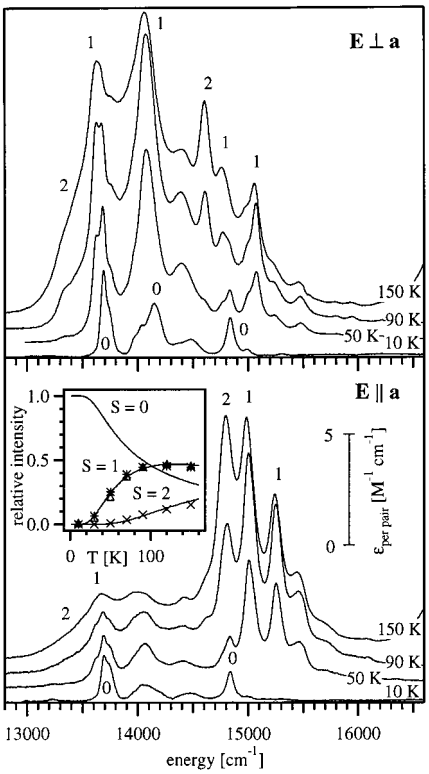

Figure 3. Single-crystal absorption spectra in $E\perp a$ (top graph) and $E\|a$(bottom graph) polarizations in the region of the $^4A_2 \rightarrow {}^2E$, $^2T_1$ single excitations in $[Cr_2L_3](ClO_4)_2Cl\cdot H_2O\cdot MeOH$ at four different temperatures. $E\perp a$ and $E\|a$ correspond to the molecular polarizations perpendicular and parallel to the Cr−Cr axis, respectively. The *S* numbers indicate the spin of the initial ground state level. The inset shows the temperature dependence of the intensity of the following $^4A_2 \rightarrow {}^2T_1$ absorption bands compared to the calculated Boltzmann distribution (solid lines) within the ground state spin levels for a Heisenberg $J_{exp} = 78$ cm^{-1}: ×, $^5A_1' \rightarrow {}^5A_2''$ ($^2T_1$) at 14800 cm^{-1}; *, $^3A_2'' \rightarrow {}^3A_1'$ ($^2T_1$) at 15000 cm^{-1}; Δ, $^3A_2'' \rightarrow {}^3A_2''$ ($^2T_1$) at 15255 cm^{-1}.

Table 2. Energies (cm^{-1}), Predominant Polarizations, Temperatures (K), and Assignment (in D_{3h}) of the Observed Transitions to Dimer Levels Observed in $[Cr_2L_3](ClO_4)_2Cl\cdot H_2O\cdot MeOH$[a]

no.	energy	polarizn	temp	assignment
1	13320	$E\perp a$	70	$^5A_1' \rightarrow {}^5E'$ (^2E)
2	13617	$E\perp a/E\|a$	30	$^3A_2'' \rightarrow {}^3E''$ (^2E)
3	13695	$E\perp a/E\|a$	10	$^1A_1' \rightarrow {}^3E''$ (^2E)
4	14080	$E\perp a$	50	$^3A_2'' \rightarrow {}^3E'$ (^2E)
5	14160	$E\perp a/E\|a$	10	$^1A_1' \rightarrow {}^3E'$ (^2E)
6	14600	$E\perp a$	70	$^5A_1' \rightarrow {}^5E'$ ($^2E(^2T_1)$)
7	14765	$E\perp a$	50	$^3A_2'' \rightarrow {}^3E''$ ($^2E(^2T_1)$)
8	14800	$E\|a$	70	$^5A_1' \rightarrow {}^5A_2''$ ($^2A_2(^2T_1)$)
9	14840	$E\perp a/E\|a$	10	$^1A_1' \rightarrow {}^3E''$ ($^2E(^2T_1)$)
10	15000	$E\|a$	50	$^3A_2'' \rightarrow {}^3A_1'$ ($^2A_2(^2T_1)$)
11	15075	$E\perp a$	50	$^3A_2'' \rightarrow {}^3E'$ ($^2E(^2T_1)$)
12	15255	$E\|a$	50	$^3A_2'' \rightarrow {}^3A_2''$ ($^2A_2(^2T_1)$)

[a] The lowest temperature at which a given transition is observed is indicated.

different from the absorption spectrum. The trap emission shows a progression with a frequency of 152 cm^{-1} based on an origin at 12880 cm^{-1}. This indicates that it is most probably due to a small impurity of a Cr^{3+} species in which the ligand field is so much reduced that the $^4T_2$ state becomes the lowest excited state. Figure 4b shows a comparison of the 20 K luminescence spectrum after excitation at 19436 cm^{-1} with the 70 K absorption spectrum in $E\perp a$ polarization, which will be discussed in section 5.1. The single-crystal absorption spectra of complex **2** in σ and π polarizations are shown in Figure 5 in

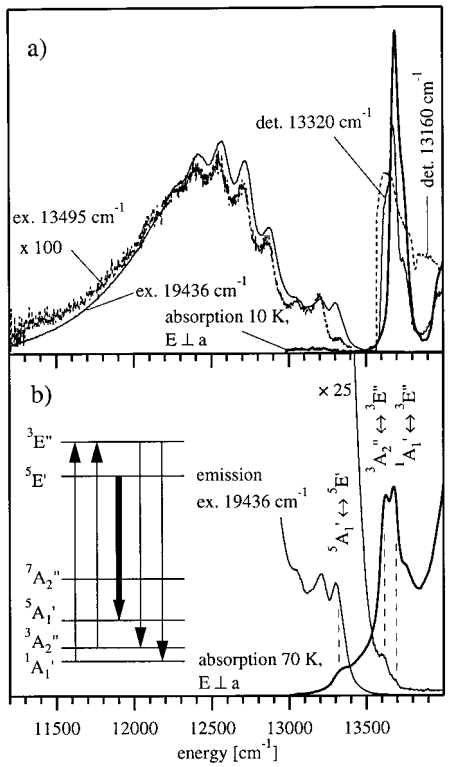

Figure 4. (a) 20 K luminescence spectra after excitation at 19436 cm^{-1} (solid line) and 13495 cm^{-1} (dotted line) are shown on the left. On the right are shown 20 K excitation spectra detecting luminescence at 13320 cm^{-1} (solid line) and 13160 cm^{-1} (dotted line). The 10 K absorption spectrum in $E \perp a$ polarization is shown as a thick solid line. (b) Comparison of absorption and luminescence spectra in the region of the lowest-energy transitions. The electronic transitions are assigned in D_{3h} notation. The energy level diagram including the observed transitions is shown on the left.

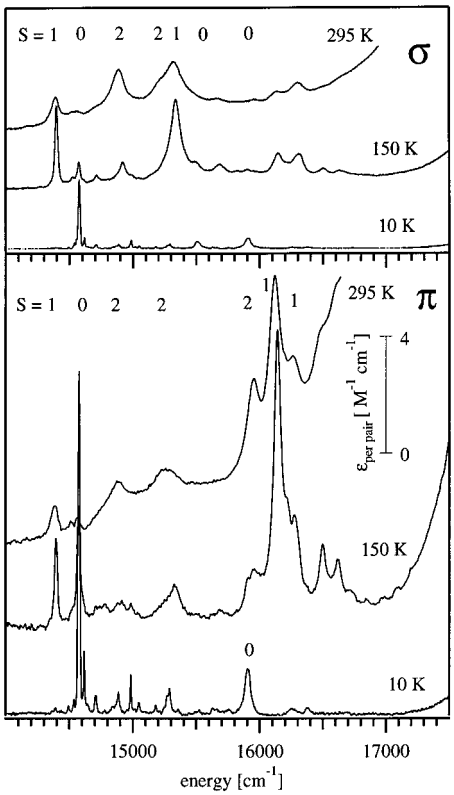

Figure 5. Single-crystal absorption spectra at three different temperatures in σ ($E \perp c$) and π ($E \| c$) polarizations of $[Cr_2(OH)_3(tmtame)_2](NO_3)_3$ **2** in the same spectral region as for the title compound **1** in Figure 3. The *S* numbers indicate the spin of the initial ground state level.

the same spectral region as for the title compound **1** in Figure 3. They will be discussed in section 5.2.

4. The VBCI Model and Exchange Parameters

The model used to calculate energy splittings is the same that we used and reported for complex **2** in ref 4, and we only give a brief summary here. It is based on a valence bond approach, explicitly calculating interactions between electron configurations under the action of a one-electron operator. The ground, an LMCT, and a metal-to-metal charge-transfer (MMCT) electron configuration are taken into account. The energies of the lowest-energy LMCT and MMCT states relative to the ground state are parametrized by Δ and U, respectively. $R(^2E)$, $R(^2T_1)$, and $R(^2T_2)$ represent the single-ion energies of the octahedral ligand-field states ^2E, $^2T_1$, and $^2T_2$, respectively. In the approximate C_{3v} site symmetry of the Cr^{3+} ions in **1**, the t_2 orbitals are split by δ_{t_2} into two sets of orbitals transforming as a_1 and e. The octahedral e orbitals are not included in the model. The model is set up in the approximate D_{3h} pair symmetry.

Two types of interaction are considered: direct interactions between orbitals centered on the metal centers A and B, often called direct exchange, as well as indirect interactions involving ligand (L) orbitals on the sulfur ligators, often called superexchange.[18] A direct interaction between $(a_1)_A$, $(a_1)_B$ or $(e)_A$, $(e)_B$ will result in the following nonzero matrix elements, respectively:

$$h_{\sigma_{MM}} = \langle (a_1)_A | \hat{h} | (a_1)_B \rangle \quad (3)$$

$$h_{\pi_{MM}} = \langle (e_x)_A | \hat{h} | (e_x)_B \rangle = \langle (e_y)_A | \hat{h} | (e_y)_B \rangle \quad (4)$$

where e_x and e_y are the two components of the e representation, $\hat{h}$ is a one-electron operator, and the integrals in eqs 3 and 4 are electron-transfer integrals.

There exist a multitude of possible interactions between ligand and metal-centered orbitals. In order to keep the model as simple as possible, we only consider those interactions which are assumed to give the major contributions to the total exchange. The p orbitals on one of the oxygen ligators and the s orbital on the adjacent hydrogen atom in **2** are schematically shown on the right of Figure 6. All these orbitals lie in the *xy* plane formed by the three ligators. In ref 4 we only considered LMCT configurations involving ligand orbitals with π symmetry with respect to the Cr−O axis in **2.** They lie tangentially to the triangle formed by the oxygen ligators (see Figure 6) and transform as e in the approximate C_{3v} single-ion frame. In **1** the situation is more complicated: Figure 6 shows the p orbitals on one of the sulfur ligators and the adjacent carbon atom, both lying within the triangular *xy* plane. Compared to **2**, the ligator p orbitals in **1** are rotated by $\gamma - 90°$ with γ being the dihedral angles of 106−112°, see Table 1, and they are involved in bonds to the carbon. The dihedral angle is the angle between one of the Cr−S−Cr planes and the adjacent S−C direction, see Scheme 1. In addition to the π interaction via the e ligand orbitals mentioned above, a σ type interaction arises in **1** from

(18) Anderson, P. W. *Phys. Rev.* **1959**, *115*, 2.
(19) Weihe, H.; Güdel, H. U.; Toftlund, H. *Inorg. Chem.* **2000**, *39*, 1351.
(20) Vanhelmont, F. W. M.; Güdel, H. U.; Förtsch, M.; Bürgi, H. B. *Inorg. Chem.* **1997**, *36*, 5512 and references therein.
(21) Atanasov, M.; Angelov, S. *Chem. Phys.* **1991**, *150*, 383.

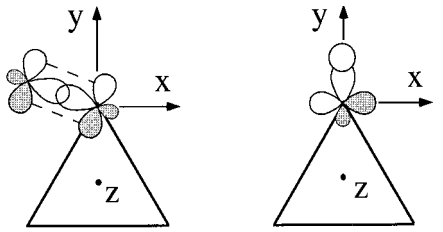

1 **2**

Figure 6. Views on the plane formed by the three bridging ligators along the Cr−Cr axis. On the left the situation for **1** is shown with the p orbitals on one of the sulfur ligators and the adjacent carbon. The corresponding situation for **2** is shown on the right with the oxygen p and the hydrogen s orbitals. *x*, *y*, and *z* define the coordinate system referred to in the text.

a possible overlap of the sulfur p orbital approximately pointing toward the *z* axis (not shown in Figure 6) with the metal-centered a_1 orbitals. However, using the angles listed in Table 1, their angular overlap is very small. Therefore the π interaction via the *e* ligand orbitals dominates the σ interaction, and we neglect the latter in our model. This allows us to use exactly the same model for **1** as presented earlier for **2**.[4] The resulting one-electron-transfer integrals for the interactions via the ligands are all equal and defined as

$$h_{\pi_{ML}} = \langle (e_x)_A|\hat{h}|(e_x)_L\rangle = \langle (e_x)_L|\hat{h}|(e_x)_B\rangle = \langle (e_y)_A|\hat{h}|(e_y)_L\rangle = \langle (e_y)_L|\hat{h}|(e_y)_B\rangle \quad (5)$$

A total of 834 pair basis functions including all three electron configurations are used for the calculation, see ref 4. They form the basis for the energy matrix which was diagonalized numerically with some of the parameters fixed and some adjustable as discussed in section 5.4.

In ref 4 we derived orbital exchange parameters J_a and J_e from our model parameters as follows:[22]

$$J_a = 4\left(\frac{h_{\sigma_{MM}}{}^2}{U}\right) \quad (6)$$

$$J_e = 4\left[\left(\frac{h_{\pi_{MM}}{}^2}{U}\right) + \left(\frac{h_{\pi_{ML}}{}^2}{\Delta}\right)^2\left(\frac{1}{U}\right)\right] \quad (7)$$

where J_a and J_e represent the exchange pathways involving the a_1 (eq 3) and *e* (eqs 4 and 5) metal-centered orbitals. These could be determined directly from experiment, but they do not offer the possibility to distinguish between direct and superexchange interactions. In the present study, however, we are interested in the comparison of the direct interactions with the interaction involving the bridging ligands. We therefore combine the three terms in eqs 6 and 7 in a different way and define exchange parameters J_{MM} and J_{ML} as follows:

$$J_{MM} = 4\left(\frac{h_{\sigma_{MM}}{}^2 + 2h_{\pi_{MM}}{}^2}{U}\right) \quad (8)$$

$$J_{ML} = 8\left(\frac{h_{\pi_{ML}}{}^2}{\Delta}\right)^2\left(\frac{1}{U}\right) \quad (9)$$

where J_{MM} takes into account the direct interactions arising from the direct overlaps of both the a_1 and *e* orbitals centered at each metal ion, whereas J_{ML} considers the superexchange pathway via the bridges involving the *e* orbitals only. The ground state exchange parameter *J* can then be expressed as a sum of two contributions J_{MM} and J_{ML}:

$$J_{model} = \frac{1}{9}(J_{MM} + J_{ML}) \quad (10)$$

Equations 6−9 are approximate, since the expansions are only taken to second order for $h_{\sigma_{MM}}$ and $h_{\pi_{MM}}$ and to fourth order for $h_{\pi_{ML}}$. However, their advantage lies in the fact that they allow us to see to what extent the different exchange interactions represented by the transfer integrals $h_{\sigma_{MM}}$, $h_{\pi_{MM}}$, and $h_{\pi_{ML}}$ contribute to J_{model}, see section 6.2.

5. Analysis

5.1. Ground State Splitting. Figure 4b provides the key for the analysis of the ground and the lowest excited state splittings. It compares the emission spectrum after excitation at 19436 cm^{-1} with the 70 K absorption spectrum in $E\perp a$ polarization. Due to its high intensity in emission and its temperature dependence in absorption, the band at 13320 cm^{-1} is assigned to an $S = 2 \leftrightarrow S^* = 2$ transition, where the star represents an excited state level. We conclude that the lowest excited level is $S^* = 2$. From the coincidence of the lines at 13617 and 13695 cm^{-1} in absorption with the weak shoulders in emission (see enlarged spectrum in Figure 4b) we assign them to $S = 1 \leftrightarrow S^* = 1$ and $S = 0 \leftrightarrow S^* = 1$ transitions, respectively. We derive the energy splitting pattern shown in the inset of Figure 4b. The singlet−triplet splitting in the ground state and thus the *J* value in the Heisenberg model are 78 cm^{-1}. A nice confirmation is provided by the temperature dependence of the intense hot bands in $E\|a$ polarization between 14800 and 15500 cm^{-1} following the Boltzmann population of the $S = 1$ and $S = 2$ ground state levels with $J_{exp} = 78$ cm^{-1}, see inset of Figure 3.

5.2. Singly Excited States. We now come to an assignment of the bands in Figure 3 to distinct pair transitions. The determination of the spin quantum numbers of the excited levels is based on intensity arguments as follows. There are two well-known intensity mechanisms for dimer transitions which are spin-forbidden in the single ion: (i) a single-ion mechanism due to the combined action of the odd-parity ligand field at the single-ion site and spin−orbit coupling; (ii) an electric-dipole exchange mechanism first proposed by Tanabe and co-workers.[23] The spin selection rule for mechanism (i) is $\Delta S = 0, \pm 1$, whereas for mechanism (ii) it is $\Delta S = 0$. The ground state spin *S* varies from 0 to 3, whereas the singly excited ^2E and $^2T_1$ pair states have S^* values of 1 and 2. Therefore cold bands can get intensity only from the single-ion mechanism, whereas hot bands may get intensity from both. As shown in Figure 3, the hot bands are about an order of magnitude more intense, nicely revealing the importance of the exchange mechanism in providing intensity. Applying the selection rule $\Delta S = 0$, we can therefore confidently determine the S^* values of the excited levels from the temperature dependence of the intense hot bands.

(22) In ref 4 an additional term $1/\Delta$ was considered in eq 7. It takes into account so-called double-LMCT transitions where two electrons are simultaneously transferred from the ligand to each of the centers A and B. Since such double-LMCT configurations are not considered in our model, we omit this term here.

(23) Ferguson, J.; Guggenheim, H. J.; Tanabe, Y. *J. Phys. Soc. Jpn* **1966**, *21*, 692.
(24) Schenker, R.; Weihe, H.; Güdel, H. U. *Chem. Phys. Lett.* **1999**, *303*, 229.

Table 3. Symmetry Labels of the Dimer Levels Arising from the ^2E and $^2T_1$ Singly Excited States[a]

C_{3v}	D_{3h}			
^2E	$^3E'$	$^3E''$	$^5E'$	$^5E''$
$^2E(^2T_1)$	$^3E'$	$^3E''$	$^5E'$	$^5E''$
$^2A_2(^2T_1)$	$^3A_1'$	$^3A_2''$	$^5A_1'$	$^5A_2''$

[a] The representations in the single-ion point groups C_{3v} (O) are listed on the left. The resulting terms in the approximate D_{3h} dimer symmetry are shown on the right.

For a more specific assignment we can take advantage of the strikingly similar features in the polarized absorption spectra of **1** and **2**. The $E\perp a$ and $E\parallel a$ polarizations for **1** in Figure 3 have to be compared with σ and π for **2** in Figure 5, respectively. All the hot bands in the spectra of **1** are strongly polarized. We can therefore assign the observed bands in the approximate trigonal symmetry. All the dimer levels (in D_{3h}) arising from the ^2E and $^2T_1$ singly excited states are summarized in Table 3. In this symmetry the following electric-dipole transitions are allowed:

$$^3A_2'' \xrightarrow{E\perp a} {}^3E'' \qquad ^3A_2'' \xrightarrow{E\parallel a} {}^3A_1'$$

$$^5A_1' \xrightarrow{E\perp a} {}^5E' \qquad ^5A_1' \xrightarrow{E\parallel a} {}^5A_2'' \qquad (11)$$

According to Table 3, only two and one triplet−triplet transitions are allowed in $E\perp a$ and $E\parallel a$ polarizations, respectively. Experimentally, four and two such transitions with significant intensities are observed, see Figure 3 and Table 2. The prominent transitions are all electronic, and we conclude that the approximate D_{3h} orbital selection rules must be strongly relaxed. On the other hand, the observed clean $E\perp a$ and $E\parallel a$ polarizations indicate that the C_3 electric-dipole orbital selection rules are still obeyed: A → E and A → A in $E\perp a$ and $E\parallel a$, respectively. For convenience we label the pair levels in D_{3h} symmetry. The experimental energy level diagram thus derived from Figure 3 for **1** is shown in the middle of Figure 7. There is a prominent gap of about 650 cm^{-1} between the three lowest levels and the higher energy ones. This suggests that the lower and higher energy groups of levels arise from the ^2E and $^2T_1$ excited states, respectively. That is how far the experiment takes us. A definite assignment to distinct pair levels is based on the results of the energy calculations. It will be discussed in section 5.4 and is shown in the last column of Table 2.

5.3. Transitions in the Near UV. From a comparison of the spectra in Figure 2 with those of the free ligand and the complex in various solvents (not shown) and from its high oscillator strength of $f \approx 1$ we assign the intense broad band at 40000 cm^{-1} to a ligand-centered $\pi \rightarrow \pi^*$ transition of the aromatic ring. The four nicely resolved cold bands at 29100, 30220, 31750, and 34050 cm^{-1} are not seen in the pure ligand spectrum, and we assign them to LMCT transitions. This is also supported by their clear temperature dependence. We thus conclude that the energies of the lowest LMCT transitions are centered at about 32000 cm^{-1} and will make further use of this in section 5.4. The slight temperature dependence of the 40000 cm^{-1} band indicates that there are additional cold LMCT bands lying underneath. There is a weak shoulder observed at the low-energy side of the LMCT bands at ≈26500 cm^{-1}. Its energy corresponds to twice the energies of the lowest singly excited levels (see section 5.2), and its intensity is low compared to the LMCT bands. We therefore assign it to a ligand-field double excitation, corresponding to the simultaneous excitation of both ions to $^2E/^2T_1$ by a single photon. Such double excitations are well-known features in the spectra of Cr^{3+} dimers and can be very intense.[4,25]

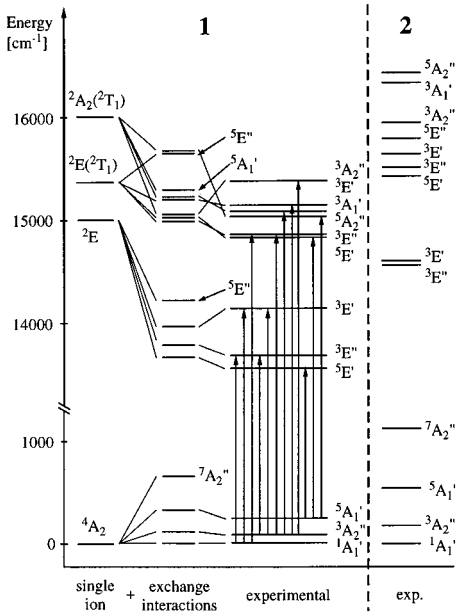

Figure 7. Energy level diagram of the ground and the $^2E/^2T_1$ singly excited states in $[Cr_2L_3](ClO_4)_2Cl\cdot H_2O\cdot MeOH$ **1**. On the left the single-ion energy levels in the absence of exchange interactions are shown. In the middle column the interactions represented by the one-electron parameters $h_{\sigma_{MM}}$, $h_{\pi_{MM}}$, and $h_{\pi_{ML}}$ are introduced. In the third column the experimental values are shown. The dimer levels are labeled in the approximate D_{3h} symmetry. The panel on the right shows the corresponding experimental splitting pattern for complex **2**.

Four LMCT bands are observed between 28000 and 36000 cm^{-1} in **1**, with comparable oscillator strengths of $f = 0.06-0.12$, see Figure 2. This is in contrast to the situation in $[Cr_2(OH)_3(tmtame)_2](NO_3)_3$, where only one intense cold LMCT band was observed at 40600 cm^{-1} with $f = 0.04$.[4] Both the significant decrease in energy and increase in intensity of these LMCT bands in **1** compared to **2** are a consequence of the increased covalency of the Cr−S compared to the Cr−O bonds. Part of the increase in intensity may be due to the aromatic π system in the ligands of **1**. The LMCT transitions borrow their intensity not only from configurational mixing with high-energy MMCT configurations[4] but also from mixing with the ligand-centered $\pi \rightarrow \pi^*$ transition. Configurational mixing between ligand-centered and charge-transfer transitions is well-known in many $(4d)^6$ and $(5d)^6$ systems containing ligands with aromatic π systems.[20] We ascribe the increased number of observed LMCT bands in **1** compared to **2** to the lowered symmetry of the dimer molecule **1**, leading to a relaxation of the orbital selection rules similar to the situation for the single excitations, see section 5.2.

5.4. Energy Calculations. We applied the model summarized in section 4 and described in ref 4 to calculate the energy splitting in the ground and ^2E and $^2T_1$ singly excited states of **1**. The following model parameter values defined in section 4 were independently determined as follows: U was fixed at 90000 cm^{-1}, the same value used for **2**[4] as estimated in ref 21. The LMCT energy Δ was set to 32000 cm^{-1}, lying at the center of gravity of the LMCT bands shown in Figure 2. The single-ion energy $R(^2T_2)$ was fixed at 20000 cm^{-1}, lowered by 1000 cm^{-1}compared to **2** as suggested from the lower Racah parameters B and C due to the increased covalency.

(25) Güdel, H. U.; Dubicki, L. *Chem. Phys.* **1974**, *6*, 272.

Table 4. Comparison of Parameter Values Obtained for $[Cr_2L_3](ClO_4)_2Cl\cdot H_2O\cdot MeOH$ (**1**) and $[Cr_2(OH)_3(tmtame)_2](NO_3)_3$ (**2**)[a]

	1	**2**		**1**	**2**
U	90000	90000	J_{exp}	78	183
Δ	32000	39000	J_{model}	66	219
$R(^2T_2)$	20000	21000	J_{MM}	262	1953
$R(^2T_1)$	15996	15536	J_{ML}	334	13.5
$R(^2E)$	15011	14947	J_{MM}/J_{ML}	0.8	144
δ_{t_2}	−1703	701			
$h_{\sigma_{MM}}$	−2057	−5723			
$h_{\pi_{MM}}$	914	−2366			
$h_{\pi_{ML}}$	−7878	−3905			

[a] The model parameters obtained from the energy fits are shown on the left, the exchange parameters on the right. J_{exp} is the experimental exchange parameter for the ground state (all values in cm^{-1}, except for J_{MM}/J_{ML}).

The single-ion energies $R(^2E)$ and $R(^2T_1)$, the trigonal splitting δ_{t_2}, and the transfer integrals $h_{\sigma_{MM}}$, $h_{\pi_{MM}}$, and $h_{\pi_{ML}}$ were obtained by a least-squares fit to the observed transitions between the $^4A_2$ ground and the ^2E and $^2T_1$ excited levels shown in Table 2. The result of the calculation corresponding to the best fit is shown in Figure 7, and the corresponding band assignments are given in Table 2. The overall agreement between calculation and experiment is good, see Figure 7. The ground state singlet−triplet splitting of 113 cm^{-1} obtained from the matrix diagonalization is in reasonable agreement with the experimentally determined value of 78 cm^{-1}. LMCT states of the lowest-energy electron configuration are calculated in the range 32000−35000 cm^{-1}, in nice agreement with the experiment. The corresponding parameter values listed in Table 4 will be discussed in the following section.

6. Discussion: Comparison between 1 and 2

6.1. Model Parameters. We now turn to a comparative discussion of the model parameters obtained for $[Cr_2L_3](ClO_4)_2Cl\cdot H_2O\cdot MeOH$ **1** with those for $[Cr_2(OH)_3(tmtame)_2](NO_3)_3$ **2** reported in ref 4, see Table 4. The MMCT energy $U = 90000$ cm^{-1} was kept at the same value for both **1** and **2**, since it only depends on the metal. In contrast, the LMCT energy Δ has dropped from 39000 cm^{-1} in **2** to 32000 cm^{-1} in **1**, as indicated by the energies of the lowest LMCT bands. This is due to the increased covalency of the Cr−S bonds in **1** compared to the Cr−O bonds in **2**. Consequently, the interaction between the ground and LMCT electron configurations parametrized by $h_{\pi_{ML}}$ is increased by 100% in **1** (Table 3), despite the enlarged metal−ligand bond lengths from Cr−O = 1.97 Å to Cr−S ranging from 2.37 to 2.44 Å, see Table 1. On the other hand, the magnitudes of both $h_{\sigma_{MM}}$ and $h_{\pi_{MM}}$ are decreased by about 60% in **1**. This is the most important difference between **1** and **2** and will be discussed in detail in section 6.2. It also results in a $S^* = 2$ level being the lowest excited level in **1**, whereas in **2** and all the other tri-μ-hydroxo-bridged dimers known so far the lowest excited state level is a $S^* = 1$.[2−4]

The single-ion energies $R(^2E)$ and $R(^2T_1)$ are increased in **1** by 64 and 460 cm^{-1}, respectively. This is in contrast to what one expects from the increased covalency, which suggests lower values for the Racah B and C parameters for sulfur compared to hydroxide ligands. This overestimation of the single-ion energies is due to the fact that in our model the effect of the increased covalency is already confirmed in the parameters Δ and $h_{\pi_{ML}}$. This effect is much stronger in **1** than in **2**, leading to the increased $h_{\pi_{ML}}$ and decreased Δ. The high covalency in **1** is responsible for the decrease of the energy of pair levels in **1** not only compared to the corresponding single-ion energies but also compared to the pair levels in **2** by about 900 cm^{-1}, see Figure 7. The large value for the trigonal parameter δ_{t_2} in **1** is partly due to the fact that it absorbs the effect of the off-diagonal trigonal parameter which was not included in the model. However, inclusion of this parameter would require specific information about the transitions to the $^2T_2$ states, which is not available experimentally either for **1** or for **2**.

From the various possible orbital exchange pathways involving the bridging ligands, only one was considered in the model. The influence of the neglected interactions is expected to increase from **2** to **1** due to the increased size of the ligand orbitals and the different geometry at the bridging ligand site, see section 4. The effects on the energy splittings of additional, neglected superexchange pathways are taken up by the existing parameters $h_{\sigma_{MM}}$, $h_{\pi_{MM}}$, and $h_{\pi_{ML}}$ and hence also by $R(^2E)$, $R(^2T_1)$, and δ_{t2}. This also leads to the reversed sign of $h_{\pi_{MM}}$ in **1** compared to **2**. We thus conclude that our simple model, originally designed for tri-μ-hydroxo-bridged Cr^{3+} dimers, is less appropriate for our tris-μ-thiolato-bridged title compound. Nevertheless, it reproduces the observed splittings very well. Although the magnitudes of the parameter values for $h_{\sigma_{MM}}$, $h_{\pi_{MM}}$, and $h_{\pi_{ML}}$ are altered by the neglect of additional superexchange pathways, they nicely follow the expected trend when going from **2** to **1**. Our model thus reproduces the fundamental differences between **1** and **2**.

6.2. Exchange Pathways. Using eqs 8−10, the model parameters can be translated into the exchange parameters J_{MM}, J_{ML}, and J_{model}, see section 4. With the values for the parameters U and Δ listed in Table 4, J_{MM} and J_{ML} and thus J_{model} are defined for the ground state. For the ^2E and $^2T_1$ excited states they would be significantly increased, due to the reduction of the denominators U and Δ in eqs 8 and 9 by roughly 14000 cm^{-1}.[4] The values for J_{model}, 66 and 219 cm^{-1} for **1** and **2**, respectively, differ by about 15% and 20% from the experimental ground state values J_{exp}, see Table 4. This reflects the approximate character of eqs 8 and 9 and thus eq 10. For **1** the neglect of additional superexchange pathways in the model may also play a role, see section 6.1. The equations allow us to examine to what extent the various interactions represented by the transfer integrals $h_{\sigma_{MM}}$, $h_{\pi_{MM}}$, and $h_{\pi_{ML}}$ (see section 4) contribute to the ground state exchange splitting represented by J_{model}. J_{MM} is decreased from 1953 cm^{-1} in $[Cr_2(OH)_3(tmtame)_2](NO_3)_3$ to 262 cm^{-1} in $[Cr_2L_3](ClO_4)_2Cl\cdot H_2O\cdot MeOH$, an enormous drop. For both **1** and **2** the σ contribution to J_{MM} is clearly dominant due to the substantial σ overlap of the a_1 orbitals pointing directly toward each other, whereas the π overlap of the e metal-centered orbitals is smaller. The effect of the strong decrease of J_{MM} from **2** to **1** on the ground state J_{model} is partly compensated by the increase of J_{ML} from 13.5 to 334 cm^{-1}, respectively. This increase by more than 1 order of magnitude is mainly due to the high polarizability of the sulfur ligand atoms, leading to a high covalency of the metal−ligand bond, resulting in the decrease of Δ and the increase of $h_{\pi_{ML}}$, see section 6.1. As a consequence, the relative importance of the direct interactions compared to the superexchange changes dramatically, as is seen from the J_{MM}/J_{ML} ratios shown in Table 4. For **2**, $J_{MM}/J_{ML} = 144$, indicating that the superexchange is clearly negligible. In contrast, in $[Cr_2L_3](ClO_4)_2Cl\cdot H_2O\cdot MeOH$ the ratio J_{MM}/J_{ML} has dropped to 0.8, i.e., the superexchange becomes comparable to the direct interactions. The different hierarchy of exchange pathways in **1** and **2** is also indicated by the polarization dependence of intensity of the hot single excitations. With reference to Figures 3 and 5, the overall

intensity ratio $E\perp a/E\parallel a$ for **1** is roughly 2/1, whereas the σ/π ratio for **2** is about 1/3. Since the hot bands gain their intensity mainly via the exchange mechanism (see section 5.2), this difference is due to the fact that the interaction between the a_1 metal-centered orbitals which gives the dominant contribution to J_{MM} only provides intensity polarized along the Cr−Cr axis, whereas the interaction via the bridges induces an electric-dipole moment with vector components both parallel and perpendicular to the Cr−Cr axis.

With reference to Figure 1 and eq 2 the strong decrease of J_{MM} from **2** to **1** can be correlated with the strong increase of the Cr−Cr distance R from 2.63 to 3.01 Å, respectively, as follows. Since both the a_1 and e metal-centered orbitals are 3d orbitals, they have the same radial dependence of the electron density. The dependence of their direct overlap on the variation of R is thus the same. Hence, in analogy to eq 2 we can write $J_{MM}/9 = \alpha e^{-\beta R}$, and eq 10 can be rewritten to

$$J_{\text{model}} = \alpha e^{-\beta R} + \frac{1}{9} J_{ML} \qquad (12)$$

We can thus separate the ground state exchange parameter J_{model} into a term only dependent on the purely geometrical parameter R, and a second term $J_{ML}/9$ which is not only dependent on the Cr−L bond lengths and Cr−L−Cr angles but also takes into account the chemical nature of the bridging ligand atoms. In Figure 1 $J_{ML}/9$ for our tris-μ-thiolate-bridged dimer corresponds to the deviation of the asterisk from the exponential curve. It suggests that the interactions via the ligands should provide the major contribution to J. A ratio J_{MM}/J_{ML} of about 1/3 for **1** is also suggested by the position of $K_3Cr_2Cl_9$ **8** in Figure 1, having a similar Cr−Cr distance R but a much smaller exchange parameter of $J_{exp} = 23\ cm^{-1}$.[15] Considering the various model approximations, the ratio $J_{MM}/J_{ML} = 0.8$ obtained from our model is in very good agreement with this.

From the exponential dependence of J on R in Figure 1 we must conclude that J_{ML} is negligible not only for hydroxide but also for fluoride ligands, that it is of minor importance for chloride and bromide bridging ligands, but that it becomes significantly important for the thiolato-bridged $[Cr_2L_3](ClO_4)_2$-$Cl\cdot H_2O\cdot MeOH$. The sulfur ligand atom is both softer and less electronegative than the bromide, chloride, hydroxide, and fluoride ligands. The covalency of the Cr−S bonds and thus the $h_{\pi_{ML}}$ value are highest, also compared to the compounds with the relatively soft bromide ligands. This then leads to a dominance of the term $(h_{\pi_{ML}}{}^4/\Delta^2)$ in eq 9.

In conclusion, with $[Cr_2L_3](ClO_4)_2Cl\cdot H_2O\cdot MeOH$ we extend the research on the exchange interactions in Cr^{3+} dimers to a tris-μ-thiolato-bridged system. Exchange splittings in the ground and singly excited states derived from polarized optical spectra were rationalized with the model developed recently for $[Cr_2(OH)_3(tmtame)_2](NO_3)_3$. It explicitly considers LMCT electron configurations and thus allows us to separate the superexchange interaction from the direct interactions. It turns out that in the tris-μ-thiolato-bridged dimer the superexchange provides a significant contribution to the net exchange, whereas it is negligible in tri-μ-hydroxo-bridged dimers. This is due to the softness of the sulfur ligand atom, leading to more covalent Cr−S bonds as indicated by the low energies of the LMCT transitions. Our model is thus in simple terms able to account for the influence of the bridging ligands on the strength and nature of the exchange coupling. The simple correlation in which the ground state exchange parameter J exponentially decreases with the Cr−Cr distance is fairly valid for triply bridged complexes with hydroxide and halide bridging ligands. In the title compound, however, superexchange is so significant that it falls outside this correlation.

Acknowledgment. Financial support from the Swiss National Science Foundation and the European Science Foundation is gratefully acknowledged.

IC001350P